OBSERVATIONS OF CORONAL STRUCTURES ABOVE AN ACTIVE REGION BY EIT AND IMPLICATIONS FOR CORONAL ENERGY DEPOSITION

W. M. NEUPERT[1], J. NEWMARK[2], J.-P. DELABOUDINIÈRE[3], B. J. THOMPSON[2], R. C. CATURA[4], J. D. MOSES[5], J. B. GURMAN[6], F. PORTIER-FOZZANI[7], A. H. GABRIEL[3], G. ARTZNER[3], F. CLETTE[8], P. CUGNON[8], A. J. MAUCHERAT[7], J. M. DEFISE[9], C. JAMAR[9], P. ROCHUS[9], K. P. DERE[5], R. A. HOWARD[5], D. J. MICHELS[5], S. FREELAND[4], J. R. LEMEN[4] and R. A. STERN[4]

[1]*Raytheon STX Corp., Lanham MD, 2070 U.S.A.**
[2]*Space Applications Corp. Vienna, VA 22180, U.S.A.*
[3]*IAS, U. Paris-Sud, Orsay, France*
[4]*LMPARL, Palo Alto, CA 94304, U.S.A.*
[5]*NRL, Washington, DC 203751, U.S.A.*
[6]*NASA-GSFC, Greenbelt, MD 20771, U.S.A.*
[7]*LAS-CNRS, Marseille, France*
[8]*ORB, Brussels, Belgium*
[9]*CSL, Liege, Belgium*

(Received 20 April 1998; accepted 19 June 1998)

Abstract. Solar EUV images recorded by the EUV Imaging Telescope (EIT) on SOHO have been used to evaluate temperature and density as a function of position in two largescale features in the corona observed in the temperature range of 1.0–2.0 MK. Such observations permit estimates of longitudinal temperature gradients (if present) in the corona and, consequently, estimates of thermal conduction and radiative losses as a function of position in the features. We examine two relatively cool features as recorded in EIT's Fe IX/X (171 Å) and Fe XII (195 Å) bands in a decaying active region. The first is a long-lived loop-like feature with one leg, ending in the active region, much more prominent than one or more distant footpoints assumed to be rooted in regions of weakly enhanced field. The other is a near-radial feature, observed at the West limb, which may be either the base of a very high loop or the base of a helmet streamer. We evaluate energy requirements to support a steady-state energy balance in these features and find in both instances that downward thermal conductive losses (at heights above the transition region) are inadequate to support local radiative losses, which are the predominant loss mechanism. The requirement that a coronal energy deposition rate proportional to the square of the ambient electron density (or pressure) is present in these cool coronal features provides an additional constraint on coronal heating mechanisms.

1. Introduction

A primary objective of the SOHO mission is the investigation of mechanisms of coronal heating. Soft X-ray instrumentation on *Skylab*, SMM, and *Yohkoh* have

*Present and mailing address: Code R/E/SE, NOAA/SEC, 325 Broadway, Boulder, CO 80303, U.S.A.

Solar Physics **183:** 305–321, 1998.

contributed much to a description of the corona at $T_e > 2$ MK and EUV instruments on the OSOs, *Skylab*, and SMM have done likewise for the transition region $T_e < 1$ MK) (see Webb, 1981, and references therein). Coronal structure between 1 and 2 MK has been less extensively studied, due primarily to the lack of appropriate emission lines in the spectral ranges of the space instrumentation. The introduction of a new technology–multilayer normal incidence optics (Walker *et al.*, 1988; Golub *et al.*, 1990) – has made it possible to achieve high spatial resolution at EUV wavelengths that was unattainable with earlier grazing incidence optics. The EIT on SOHO is the first instrument in space to apply this technology to extended observations of the Sun (Delaboudinière *et al.*, 1995). Initial scientific results of the investigation have been presented in Moses *et al.* (1997). In this paper we demonstrate that energy deposition in two large emission features scales with the square of the local electron density (or pressure). This result is contrary to the dependence expected for typical wave-mode energy deposition processes (Rosner, Tucker, and Vaiana, 1978; Craig, McClymont, and Underwood, 1978).

Observational progress in detecting the signatures of heating processes requires a concerted observing program utilizing both SOHO's spectroscopic and imaging capabilities that provide a comprehensive description of the coronal plasma, including non-thermal emission line widths, and the EIT has supported such spectroscopic investigations via Joint Observing Programs (JOPS). However, it is also useful to provide a characterization of features as recorded by EIT itself (Aschwanden *et al.*, 1998a, b). In this paper we examine two features in the temperature range of 1.0–2.0 MK that extend to heights greater than their nominal pressure scale heights in an effort to evaluate radiative and conductive energy losses and their implications for coronal energy deposition.

2. Observations

The EIT provides the capability for multi-wavelength imaging of the corona in four spectral bands, centered at 171, 195, 284, and 304 Å using multilayer telescope technology (Delaboudinière *et al.*, 1995; Moses *et al.*, 1997). These bands encompass coronal temperatures from 1 MK to 2.5 MK as well as upper chromospheric temperatures at about 60 000 K. In particular, nearly simultaneous imaging in passbands centered near 171 Å and 195 Å bands, the former including major Fe IX and Fe X emission lines, the latter including a strong Fe XII line, provides a capability to infer the morphology and characteristics of the corona at temperatures of 1.0–1.5 MK, a temperature regime below the principal sensitivity range of the Soft X-ray Telescope (SXT) on *Yohkoh*.

EIT observations of an active region at Carrington Longitude 260° were made at its initial appearance in July 1996 and continued on successive solar rotations through October (Portier-Fozzani *et al.*, 1998). By late September the region was in decline with no evidence of sunspots or flare activity (no NOAA number was

assigned) and with only dispersed magnetic fields of opposite polarity separated by a filament channel that was particularly evident in the 171 Å and 195 Å bands. To establish the three-dimensional geometry of the large-scale features over this active region remnant, we observed the region from day-to-day during its September transit. While changing in small detail over time scales of tens of minutes to hours (as verified with several seven-minute cadences of observations), the overall structure of the active region appeared to change little as it moved from the central meridian to the West limb. That stability was important as it provided the opportunity to estimate the lateral extent of features from disk observations and their range of heights from limb observations.

Figure 1 shows EIT images of the region near central meridian in the 171 Å and 195 Å bands while Figure 2 shows the same region as it neared the west limb. The image pairs were taken closely together in time (5 min or less) so that spatial shifts due to solar rotation were negligible at EIT's spatial resolution (pixel size = 2.6 arc sec). The filament channel separating opposite magnetic polarities was clearly visible on 25 September and was still discernable near the limb on 30 September. Coronal emission over this filament channel consisted principally of high loops connecting regions of enhanced magnetic field (i.e., loops over the magnetic neutral line). These loops were clearly detected in SXT soft X-ray images to a lesser extent in EIT's 284 Å (Fe XV) channel. Portier-Fozzani *et al.* (1998) discuss the evolution of these loops during the September transit of the region. Such loops are generally detectable over their entire length, have two footpoints of comparable brightness, and can have temperatures as low as 1×10^6 K (Sheeley, 1980). A three-dimensional analysis of such features has been presented by Aschwanden *et al.* (1998a).

EIT also observes features that emanate from the strong magnetic fields of an active region toward distant regions of presumably weakly enhanced field preceding and trailing the active region. Such features display obvious longitudinal brightness gradients. In such features the leg of the (presumed) loop associated with a strongly enhanced field is prominent whereas the opposite leg is often so faint that it cannot be reliably traced to a specific region of the photosphere. An example of such an asymmetric feature in the September active region is designated (a) in Figure 1. This feature varied little in its overall configuration from day-to-day and its limb appearance (Figure 2) was consistent with a system of loops as viewed in the plane of the loops, with the trailing bright footpoints visible on the disk. No fine structure that would be evidence for an array of diverging loops is present in Figure 1, although some detail was observed at other times. *Skylab* EUV observations (Sheeley, 1980) did detect fan-like collections of loops, and high resolution (1 arc sec) soft X-ray observations (Sams, Golub, and Weiss, 1992; Figure 6) show similar collections of loops emanating from the penumbra of a large sunspot. Feature (a) may therefore alternatively be interpreted as a bundle of loops diverging from a compact region associated with an enhanced photospheric magnetic field in the active region but connecting to distant and well separated footpoints in regions

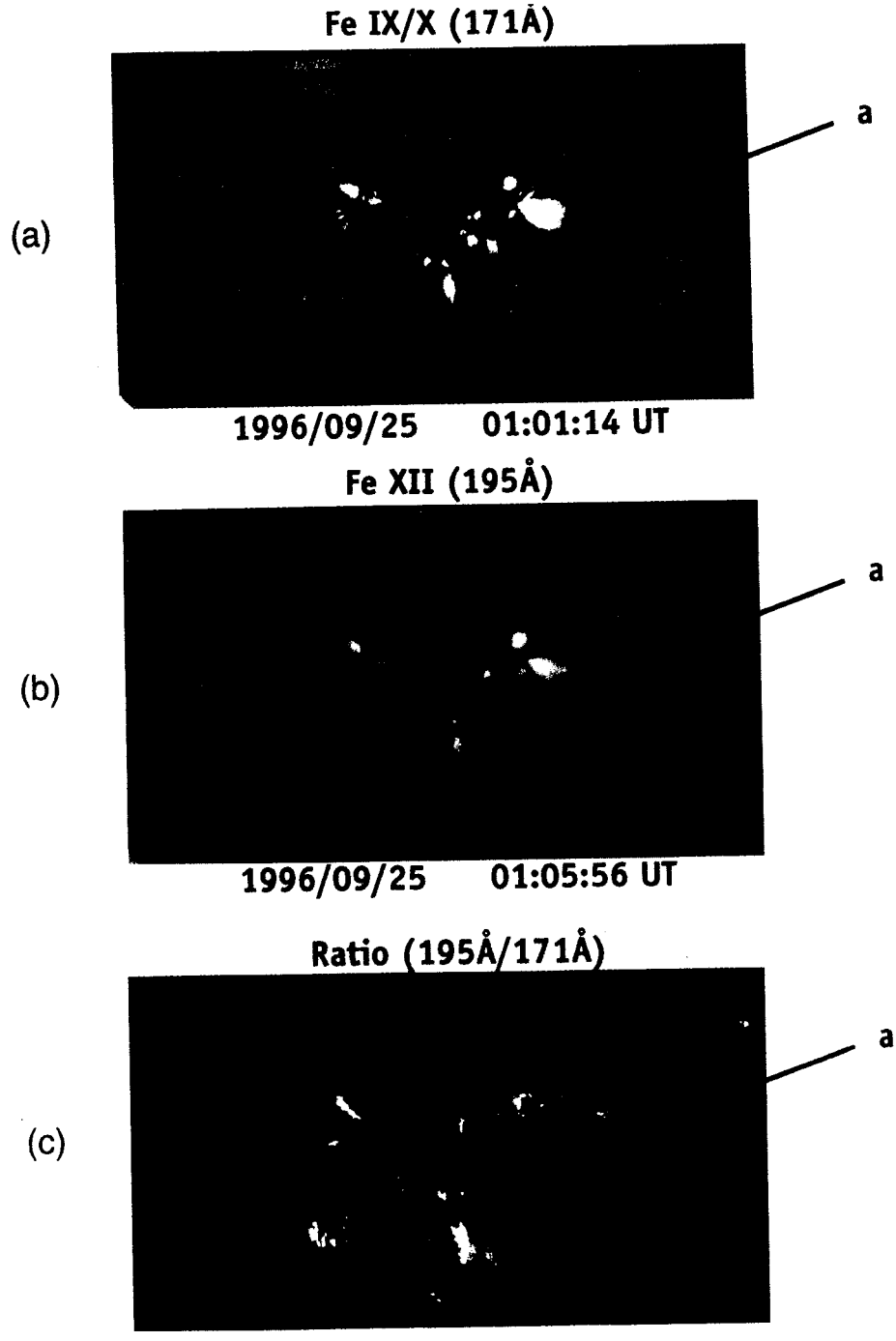

Figure 1. Observations of a decaying active region near the Central Meridian on 25 September 1996. (a) Fe IX/X emission; (b) Fe XII emission; (c) Ratio of the Fe XII and Fe IX/X images. The angular field of view of each image is 640 × 1140 arc sec. A coronal loop feature selected for analysis is indicated. Two blocks of uniform color near the centers of frames (b) and (c) are fillers for data that are missing.

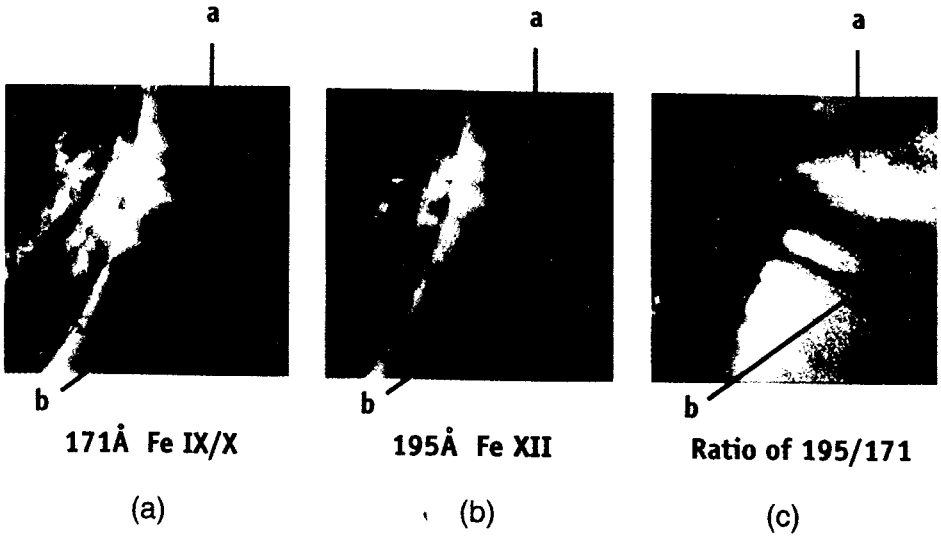

Figure 2. Observations by of a decaying active region approaching the west limb on 30 September 1996. (a) Fe IX/X emission; (b) Fe XII emission; (c) Ratio of the Fe XII and Fe IX/X images. As in Figure 1, increasing brightness in the ratio implies increasing T_e from approximately 1.0 MK to [illegible] MK. The angular field of view of each image is 582 × 582 arc sec. Two features selected for [illegible] ysis are indicated.

of weakly enhanced magnetic field. Fe XV images were obtained about 5 hours prior to the 25 September data set and appeared to have a more diffuse morphology probably not cospatial with the Fe IX/X and Fe II features.

In addition to loops over the neutral line and the loops directed away from the region, EIT recorded during west limb passage of the region an extended ray-like feature with no obvious curvature or second footpoint. This feature is designated (b) in Figure 2. Its appearance in the limited EIT field of view was consistent with either an extended loop closing far above the field of view or a near-radial open field region, as might be present at the base of a helmet streamer. The latter interpretation is supported by data returned from the LASCO CI coronagraph (S. Plunkett, 1996, private communication). Feature (b) was observed as a darker feature (diminished emission) in Fe XV, indicating that its T_e could not have exceeded approximately 2×10^6 K.

3. Analysis

3.1. Calculation of Coronal Temperatures and Emission Measures

As the formation temperatures of lines in the Fe IX/X and Fe XII bands are similar (ionization peaks near 0.8–0.9 and 1.4 MK), the ratio of these bands can provide an estimate of T_e, given the assumption that the plasma is near-isothermal and

cospatial. These ratios are displayed in frames (c) of Figures 1 and 2 where increasing brightness implies increasing T_e. Newmark (1996) has convolved hypothetical EUV spectra provided by the CHIANTI program (Dere *et al.*, 1997) with the measured passbands of each of EIT's three coronal channels to derive T_e and emission measure of an assumed isothermal plasma as functions of the signal levels in pairs (171 Å and 195 Å or 195 Å and 284 Å) of EIT images. The 'eit-temp' routine in the EIT data analysis library was used for determination of temperatures and emission measures. Several sources of uncertainties in the results must be addressed first, however.

3.2. Error Analysis

Klimchuk and Gary (1995) have made an error analysis of both random and systematic errors associated with the SXT measurements (as have Kano and Tsuneta, 1995; Porter and Klimchuk, 1995). Application of a similar approach is appropriate for the EIT image ratios and we base our error estimates on Equations (3.1)–(3.5) of their paper. Tarbell (1996) has determined that the photon noise is between $0.7(DN)^{1/2}$ and $0.95(DN)^{1/2}$ as each data unit (DN) corresponds to more than one arriving photon, the actual value being between 4 and 6. As a conservative approach we adopted a value of $1(DN)^{1/2}$. In addition there is a residual noise level of approximately $7^{1/2}$ due to readout noise and unsubtracted cosmic rays associated with each data readout, so that

$$(\text{noise})^2 = 7 + S\,, \tag{1}$$

where S is the signal level. The uncertainty associated with each emission ratio and hence temperature includes contributions from four data values (two for each wavelength – a feature signal and a fore/background signal from the adjacent corona).

Systematic errors in the analysis of EIT data include (a) uncertainties in the initial calibration, particularly in determining the spectral response in the far wings of the instrument's spectral passbands, (b) time-dependent EUV absorption at the surface of the cold CCD due to adsorption of volatiles, and (c) uncertainty in the location-dependent electron/photon production ratio in the CCD and its degradation with time (Defise *et al.*, 1997). The calibration used in this paper is based on the preflight calibration, flatfielding corrections to remove artifacts produced by the filter support mesh, and adjustments of up to 30% to compensate for estimated in-orbit degradation. At present, the uncertainty in sensitivity may be as high as a factor of four (yielding factors of two uncertainties in density estimates). Work is in progress to improve the EIT calibration using data from a recent EIT calibration rocket flight.

Additional sources of uncertainty are the result of EIT's limited spatial resolution, uncertainties in the geometries of features, and subtraction of emission along the same line of sight but not emanating from spatially resolved feature

fore/background emission. We assumed the level of this extraneous emission to be the same as emission from adjacent regions that appeared to be structureless but not anomalously faint. An accurate subtraction of the ambient (i.e., unenhanced) corona is especially difficult above the solar limb because of the steep radial gradients in coronal emission and the lack of nearby featureless regions. For that reason disk observations were preferable for analysis of feature (a). For near-radial features, as our feature (b) appears to be, only limb observations can provide the required spatial distribution of emission. With diminishing feature brightness (as may occur with increasing distance from the solar limb), the nominal fore/background correction becomes comparable (up to 80%) to the total signal which introduces a major uncertainty at low signal levels.

4. Results

4.1. Electron Temperature and Density Distributions

4.1.1. *High Loop System*

A qualitative distribution of temperature (within the limited 1–2 MK range) for feature (a) is displayed in Figure 1(c). Darker areas correspond to cooler regions ($\simeq$ 1.0–1.2 MK) while the brightest regions are in the 1.4–1.6 MK range. Observations on both 25 September and 30 September for feature (a) display a gradient from darker to light shades along its length, indicating increasing temperature as the line of sight moves away from the loop footpoint, with most of the increase appearing in the upper $\frac{1}{3}$ of the feature. Fluctuations across the feature were minor compared to the longitudinal change. The inferred coronal temperatures as a function of distance from the active region footpoint (derived from disk observations) of feature (a) are shown in Figure 3 together with a hand-fitted (dashed) curve. The plot assumes a semicircular loop of height 100 000 km with a temperature maximum at its apex. Temperature gradients range from 0.41 K km^{-1} at the lowest coronal heights observed to 10 K km^{-1} immediately below the loop apex. To provide an estimate of the impact that the uncertainty in fore/background coronal correction may have on our results, we also indicate in Figure 3 the temperature that would be inferred if no correction for fore/background emission were applied. Vertical error bars for points that include a fore/background correction are ± 3 standard deviations. Horizontal (dashed) error bars represent estimated positional uncertainties of ± 5 pixels (9100 km) in footpoint location and ± 10 pixels (18 200 km) in apex location). These uncertainties are equivalent to uncertainties in loop radii and apex heights of $\pm 20\,000$ km. The error in relative calibration between the 171 Å and 195 Å channels is estimated to be no greater than 40%. An error of that magnitude would correspond to a temperature shift of approximately 100 000 K for all points because of the near-linearity of signal ratio with T_e. An additional uncertainty in establishing the spatial scale is the unavoidable summation of emission

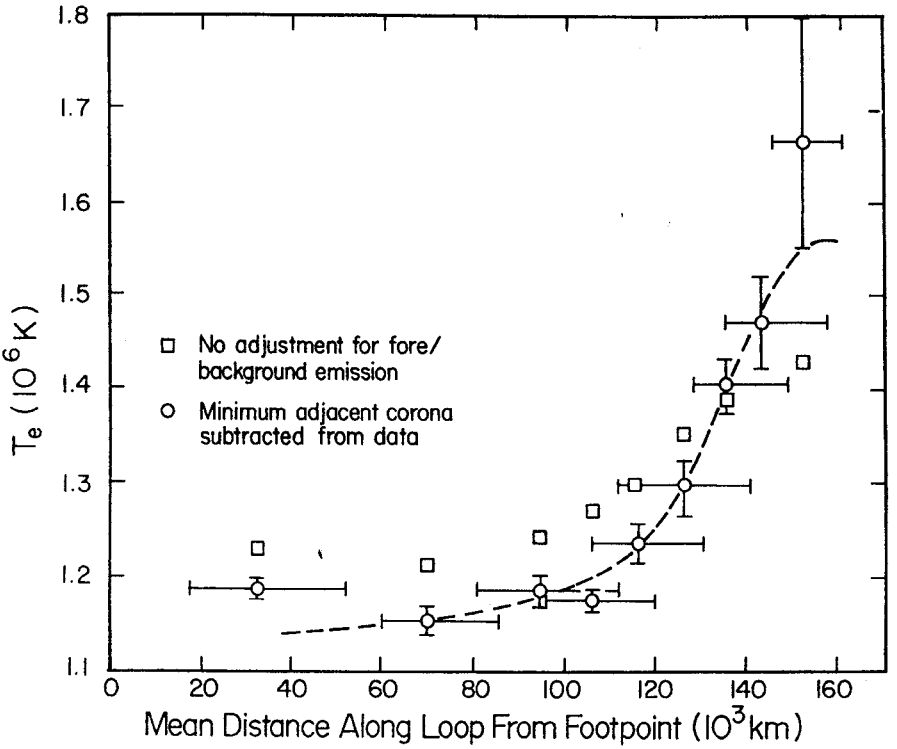

Figure 3. Temperature as a function of distance along loop feature (a), for an assumed semicircular loop of height 100 000 km, from disk observations in the Fe XII and Fe IX/X bands on 25 September 1996. Circular data points include a correction for fore/background emission along each line of sight whereas the open squares do not.

along oblique lines of sight through the feature and therefore over a range of heights and, in our models, a range of distances from the assumed footpoints. That range corresponds to 60–70% of the nominal footpoint distance for the lowest data point and 30% for the highest. These ranges are not included in the error (uncertainty) bars for distances shown in Figure 3. The distances used in that figure correspond to distances along the assumed axis of the broad observed feature.

The average electron density along a line of sight through the modeled loop is assumed to be

$$n_e = (\mathrm{EM}/L\phi)^{1/2} \quad [\mathrm{cm}^{-3}], \tag{2}$$

where EM is the line-of-sight emission measure from the eit-temp data analysis routine, L is the distance through the loop along the line of sight, and ϕ is the fill factor, the fraction of the observed volume that contains emitting material (Cargill and Klimchuk, 1997). As mentioned in Section 1, feature (a) may be interpreted as a single loop or as an ensemble of unresolved loop structures within the envelope of the observed feature. In the latter case, we assumed an ensemble of loops or strands

tightly bunched together at the bright footpoint only and connected to widely separated distant footpoints so that the fractional volume, ϕ, actually occupied by the ensemble of strands decreased with increasing distance from the footpoint, depending on the expansion factors of the individual strands. That geometry is consistent with early results from *Skylab* (Sheeley, 1980) and with observations of loops rooted in the penumbra of a large sunspot (Sam, Golub, and Weiss, 1992; Figure 5(a)). We will examine both hypotheses as a means of estimating the likely range of loop densities and local heating requirements.

For both cases the total width of the loop system, w, as a function of distance, s, from the footpoint was modeled from observations near central meridian as:

$$w = 11\,000 + 0.32s \quad [\text{km}] . \tag{3}$$

Table I summarizes coronal densities assuming the feature is a single semicircular expanding loop with a circular crossection corresponding to its observed width. The obliquity of the line of sight through the loop for each observation was taken into account. This model is not likely to be realistic as we observe no symmetry of emission about a loop apex. Furthermore, the expansion factor (ratio of thickness at apex to thickness at footpoint) of 5.6 is far larger than would be expected for a dipole magnetic configuration (Klimchuk *et al.*, 1992). It does, however, represent a hypothesis for which we can evaluate the terms of the energy equation. Table II summarizes fill factors and densities as a function of distance from the footpoint for the multiple loop hypothesis, assuming that the loops originated in a footpoint area with a diameter of 6 EIT pixels (11 000 km) and that they diverged with height (each maintaining a constant crossectional area) so as to be spaced uniformly within the entire volume that we associate with the feature (i.e., the cross-sectional areas used in Table I). Such a hypothesis would explain the apparent brightness asymmetry of feature (a) as being the result of EIT's limited spatial resolution combined with a rapidly diminishing fill factor.

The densities given in Tables I and II are subject to limitations in determining the sizes of the emitting structures. An estimated error of two pixels (33%) in the six-pixel footpoint diameter has no impact on the single-loop densities in Table I, where loop dimensions above the footpoint are measured independently (again with an estimated error of two pixels – about 20% – resulting in a density uncertainly of 10%). In the case of multiple loops – Table II – the greater error in the footpoint diameter propagates to all heights as an error in the fill factor. The effect of these uncertainties on estimated densities is small compared to the present factor of four uncertainty in the EIT calibration (and hence a factor of four in radiative losses) discussed earlier and will not alter the conclusions regarding energy balance to be discussed in Section 4.2.

The inferred pressure scale height is dependent on the details of the assumed model. For the single loop model the inferred pressures are consistent with a scale height of 50 000 ± 10 000 km. For the multiple loop hypothesis, the densities (and pressures) within the compact loops remain approximately constant with height.

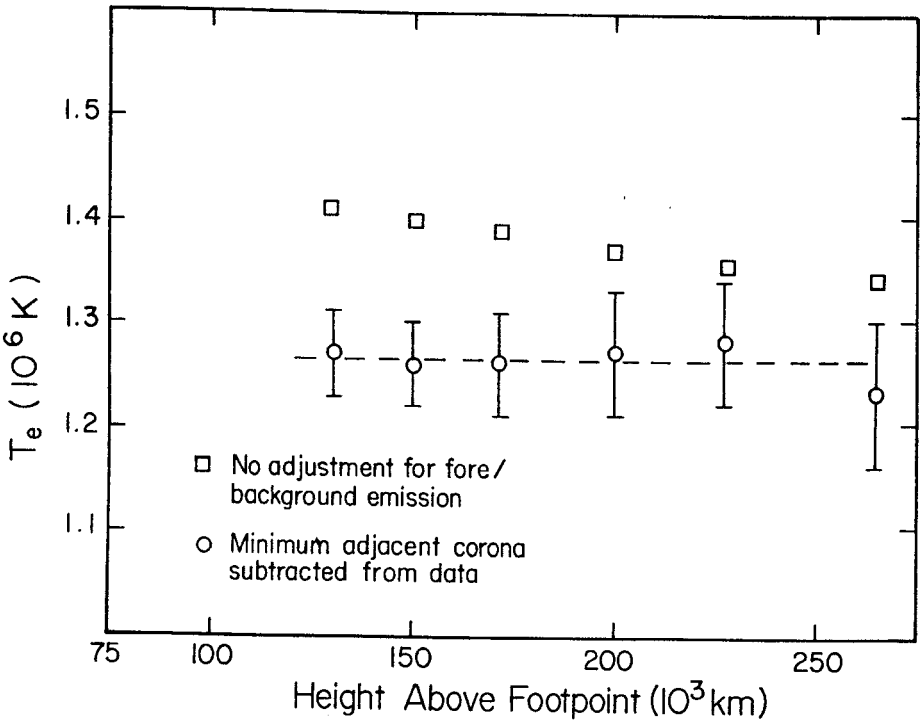

Figure 4. Temperature distribution along a near-radial feature as observed on the west limb on 30 September 1996. Circular data points include a correction for fore/background emission whereas open squares do not. The results are consistent with an isothermal distribution with height (or even a slight negative gradient, if no background correction is applied).

These results are to be compared with the expected scale height of 60 000 km ($(5000 \times T_e)$ km). By comparison, for loops hotter than the EIT loops but in the same range of heights (100 000 km), Kano and Tsuneta (1995) found densities and pressures to be 2–3 times higher at loop tops than at their bases.

4.1.2. *Extended, Near-Radial Feature*

In contrast to the T_e gradient found in the high loop system, the near-radial feature (b) exhibits no significant outwardly increasing temperature as may be seen qualitatively in Figure 2, frame (c), where the ratio appears as a nearly uniform dark feature out to the greatest distance observable by EIT.

Resulting temperatures are shown in Figure 4. There may even be a slight negative gradient of 0.6 K km^{-1} with height if no fore/background correction is applied. Feature (b) was not precisely aligned with any emission region on the solar disk and may have been rooted in an area already behind the west limb, making estimation of heights above the chromosphere somewhat ambiguous. That uncertainty is estimated to be $\pm 15\,000$ km and has negligible impact on the following discussion.

For an equatorial coronal hole Withbroe's radiative energy balance model (1988, his Figure 2) yields a broad temperature maximum near $R = 2\ R_\odot$, well beyond the heights of our observations. For the unstructured corona (his Figure 11), which may be more appropriate to the current observations, the maximum is near $R = 1.2\ R_\odot$ and not inconsistent with our data. Adopting a circular crossection with diameter increasing as $R/R_\odot$ and with an area of 1.37×10^{18} cm^2 at a height of 150 000 km, we find the properties listed in Table III. The results imply a pressure (and density) scale height of 170 000 km, far greater than is expected.

4.2. LOCAL ENERGY BALANCE

We adopt the equations for energy and mass conservation in a coronal plasma as stated by Kopp and Orrall (1976) and Withbroe (1988), among others:

$$\Phi N_e N_p + \frac{1}{A(r)} \frac{\mathrm{d}}{\mathrm{d}r} \left\{ A(r)[F_c + F_m + F_A] + \lambda \left[\frac{5kT}{2m\mu} + \frac{V^2}{2} - \frac{GM_\odot}{r} \right] \right\} = 0 \quad (4)$$

and

$$\lambda = \rho V A(r)\ , \quad (5)$$

where the terms denote radiative losses, the divergence of the conductive, mechanical, and Alfvén wave fluxes, and the divergence of the enthalpy, kinetic energy and potential energy. ρ is the density in g cm^{-3} and V is the velocity through the area $A(r)$.

Evaluating all the possibly significant terms for EIT features is clearly impossible. Brekke *et al.* (1997) have used the CDS on SOHO to demonstrate the presence of flows in at least some coronal loops, but no data are available for the features that we discuss here. Although a mechanical flux is likely present (as evidenced by the ubiquitous non-thermal broadening of spectral lines), we have no information on changes of non-thermal broadening with height and hence the divergence of the mechanical flux. Downflows of 10 km s^{-1} at transition region temperatures have typically been observed and have been the basis for estimating downward enthalpy fluxes in the chromosphere – corona transition region (Pneuman and Kopp, 1977). However, their results have not been confirmed for the coronal components of a loop and we have therefore chosen to ignore possible enthalpy flows.

Local radiative losses were derived from:

$$\Phi N_e N_p = \Phi \frac{\mathrm{EM}}{\phi L} \quad [\mathrm{erg\ cm^{-3}\ s^{-1}}] \quad (6)$$

where Φ is the radiative loss function at T_e (we used $\Phi = 1.9 \times 10^{-22}$ erg cm^3 s^{-1} (Cargill and Klimchuk, 1997)).

Conductive losses were calculated by

$$\mathrm{div}\ F_c = \frac{\kappa_0}{A(s)} \frac{\mathrm{d}}{\mathrm{d}s} \left[A(s) T^{5/2} \frac{\mathrm{d}T}{\mathrm{d}s} \right] \quad [\mathrm{erg\ cm^{-3}\ s^{-1}}]\ , \quad (7)$$

TABLE I

Energy losses an input requirements assuming a single large loop (apex width / loop length = 0.2)

Distance from footpoint (km)	T_e (MK)	ϕ	n_e	P^*_{rad}	div F^*_c	Nonthermal energy input rate*
45 000	1.14	1.0	1.2×10^{9}	3×10^{-4}	-3.4×10^{-6}	3×10^{-4}
70 000	1.15	1.0	1.2×10^{9}	3×10^{-4}	-4.4×10^{-6}	3×10^{-4}
100 000	1.185	1.0	0.9×10^{9}	1.6×10^{-4}	-2.5×10^{-5}	1.4×10^{-4}
130 000	1.34	1.0	0.6×10^{9}	5.9×10^{-5}	-10.5×10^{-5}	≈ 0

*Units of erg cm^{-3} s^{-1}.

TABLE II

Energy losses and input requirements assuming diverging loops of constant crossectional area

Distance from footpoint (km)	T_e (MK)	ϕ	n_e	P^*_{rad}	div F^*_c	Nonthermal energy input rate*
45 000	1.14	0.19	2.9×10^{9}	1.6×10^{-3}	-1.6×10^{-6}	1.6×10^{-3}
70 000	1.15	0.11	3.5×10^{9}	2.3×10^{-3}	-2.2×10^{-6}	2.3×10^{-3}
100 000	1.185	0.065	3.6×10^{9}	2.5×10^{-3}	-1.9×10^{-5}	2.5×10^{-3}
130 000	1.34	0.044	2.6×10^{9}	1.4×10^{-3}	-7.9×10^{-5}	1.4×10^{-3}

*Units of erg cm^{-3} s^{-1}.

where $\kappa_0 = 1.1 \times 10^{-6}$ and s is the distance along the feature from its base.

If a feature is magnetically open to the heliosphere, so that an outward flow is present, then work against gravity is given by

$$\frac{\lambda}{A(r)} \frac{\mathrm{d}}{\mathrm{d}r} \left(\frac{GM_\odot}{r} \right) = 2.25 \times 10^{5} \left(\frac{R_1}{R} \right) \quad [\text{erg cm}^{-3} \text{ s}^{-1}] \,, \tag{8}$$

where G is the gravitational constant and $M_\odot$ is the solar mass. This term will be considered only for feature (b) and is discussed in Section 4.2.2.

4.2.1. *High Loop System*

The contributions of radiative and conductive losses to the energy balance for the two models of the loop system are summarized in Tables I and II. Uncertainties in the maximum height and T_e of the feature have little effect on its properties at intermediate heights as can be seen by inspection of the estimated error bars (Figure 3). Because of the near-linearity of temperature as a function of signal ratios between 1.0 and 2.0 MK, the impact of calibration errors on temperature gradients, hence conductive fluxes and div F_e is minor. The maximum (40%) error in relative calibration of the Fe IX/X channel relative to the Fe XII channel discussed earlier would result in a 10% error in F_e and a 20% error in div T_e. The resulting change

TABLE III

Energy losses and input requirements in a near-radial feature

Distance from footpoint (km)	T_e (MK)	n_e	Radiative loss*	Work against gravity*	Nonthermal energy input rate*
130 000	1.27	4.7×10^8	4.5×10^{-5}	2.4×10^{-5}	6.9×10^{-5}
150 000	1.26	4.2×10^8	3.3×10^{-5}	2.2×10^{-5}	5.5×10^{-5}
170 000	1.26	3.2×10^8	2.0×10^{-5}	2.0×10^{-5}	4.0×10^{-5}
200 000	1.27	2.9×10^8	1.6×10^{-5}	1.8×10^{-5}	3.4×10^{-5}
230 000	1.28	2.5×10^8	1.2×10^{-5}	1.6×10^{-5}	2.8×10^{-5}
265 000	1.23	2.2×10^8	0.92×10^{-5}	1.4×10^{-5}	2.3×10^{-5}

*Units of erg cm^{-3} s^{-1}.

in radiative flux would be negligible because of the near-constancy of the radiative loss function with temperature at these coronal temperatures. Adopting a coronal loop model with a fill factor less than one (Table II) increases radiative losses relative to conductive losses, but radiative losses are the major loss mechanism in both loop cases. Using the EIT observations with no adjustment for extraneous line or continuum emission (Section 3.2) would reduce temperature gradients and conductive losses relative to radiative losses, thereby only re-enforcing the predominance of radiative losses. Wheatland, Sturrock, and Acton (1997) have argued that energy deposition at the tops of the hot loops recorded by SXT can by downward thermal conduction support energy losses below the loop apex. That conclusion is inconsistent with our present results for these cooler loops. A downward conductive flux does exist, but the divergence of that flux is adequate to heat the corona only immediately below the apex and then only in the low density case, as represented in our single loop model. Over the larger longitudinal extent of the loops only a volumetric heating rate distributed over the length of the loops and proportional to n_e^2 can match the energy requirements of these cool loops.

4.2.2. *Extended, Near-Radial Feature*

The significant terms in the energy balance for the apparently open feature are summarized in Table III. The lack of a temperature gradient in the extended ray implies that conductive losses again play a negligible role in coronal heating far above the transition region. To evaluate the work required to lift the plasma, if this feature does in fact extend to the heliosphere, we adopted a solar wind velocity of 400 km s^{-1} at $R_1 = 1.21\ R_\odot$ (about twice the value given by Withbroe (1988, his Figure 11 and Table II) for an unstructured region in the corona) and mass flux conservation in a ray whose crossectional diameter increased as $R/R_\odot$. We used a helium/hydrogen abundance of 0.1 giving $\rho = 1.17\ n_e m_p$. Under these assumptions energy requirements to lift the plasma become larger than radiation

losses at heights of $R \geq 1.24\ R_{\odot}$. Feldman *et al.* (1997) have proposed that far higher velocities may be present at these heights in a polar coronal hole if explosive jets of matter initiate the fast solar wind and if such were present here (none were observed in high rate observations of this feature) the energy balance would be appreciably altered. If a strong solar wind is not present, then the observations are again consistent with a volumetric heating rate proportional to the square of the local electron density.

5. Discussion

5.1. Energy input requirements

Any discussion of energy input hangs on the assumption that a quasi-steady energy deposition process (or possibly more than one) is present. Previous studies (Klimchuk and Porter, 1995; Yoshida and Tsuneta, 1995) have concluded that lifetimes of soft X-ray emitting loops are long compared to estimated energy loss times and the results of Arndt, Habbal, and Karouska (1994) indicate that coronal structures in the temperature range being discussed here (1–1.5 MK) may have less variability than either cooler (1×10^5 K) or hotter features. Aschwanden *et al.* (1998b) have discussed a statistical model for heating large EIT loops and concluded that localized transient heating at a mean rate of about 5 min at any location could maintain the temperature gradients they observe. The divergence of loops in feature (a) (or the broadening of a single loop) and their connections to distant and widely separated chromospheric regions would seem to be incompatible with a twisting together of field lines leading to reconnection and localized heating. We suggest that a process associated with the bright footpoint area, i.e., the active region end of the loops, is responsible for the propagation of energy into the coronal fields of the observed loop system.

Estimates of time-averaged total energy input rates at the bases of features (a) and (b) can be made by integrating estimated losses over the volume of each feature. For loop feature (a), the resulting estimate scales inversely with the base area adopted for the loop system. Taking into account the convergence of feature (a) with decreasing height (a factor of 42 in cross-sectional area between apex and base), we find that an energy input rate of 2×10^7 erg cm^{-2} s^{-1} at the base of corona is required to maintain the observed loop system. The estimated error in this result is the same as that of the base area, 75%, discussed earlier. Our result is greater than the early estimate of 5×10^6 erg cm^{-2} s^{-1} given by Withbroe and Noyes (1977) for radiative losses. The discrepancy could be due either to present errors in estimating the footpoint size, errors in EIT calibration, or the lower spatial resolution of observations on which the earlier estimates were based. Of course, another distributed heating process such as 'nanoflares' may satisfy the observed EIT loop characteristics and for such a process the estimation of mechanical energy flows at the coronal base made above would not be appropriate.

Energy requirements at the base of the near-radial feature depend strongly on whether or not an energy input to support the lifting of the plasma (and acceleration at higher levels in the corona) is required. The energy input to support radiative losses over the height range observed is about 1×10^6 erg cm^{-2} s^{-1}. Gravitational work to the greatest height observed is an order of magnitude less. This result is to be compared with Withbroe and Noyes' (1977) estimates of radiative and solar wind flux requirements of $1-2 \times 10^5$ erg cm^{-2} s^{-1} for the quiet Sun and 7×10^5 erg cm^{-2} s^{-1} for coronal holes.

5.2. Dependence of Energy Deposition on Ambient Pressure or Mass Density

Beginning with Rosner, Tucker, and Vaiana (1978) and Craig, McClymont, and Underwood (1978), and continuing through recent efforts by Klimchuk and Porter (1995), numerous authors have examined the dependence of various heating models in terms of observable coronal parameters. The single loop feature that we have discussed falls consistently (particularly for model 1) at the extreme range of halflengths for SXT loops (Klimchuck and Porter, 1995, Figure 1) and we conjecture that our feature may follow the same functional relationship uncovered by Klimchuck and Porter (1995):

$$P \sim L^{\beta} , \tag{9}$$

where β has a most probable value of -0.96.

Klimchuck and Porter introduce the average volumetric heating rate:

$$\langle \mathcal{Q} \rangle \sim P^{14/(11-2b)} L^{(4b-8)/(11-2b)} , \tag{10}$$

where $b = -\frac{3}{2}$ is appropriate for the EIT loops. Combining these relationships into the form

$$\langle \mathcal{Q} \rangle \sim L^{a} , \tag{11}$$

they find that a has the most probable value of -1.95.

Combining these two results, we find:

$$\langle \mathcal{Q} \rangle \sim p^{\alpha/\beta} = p^{2.05} , \tag{12}$$

i.e., average energy deposition for an isothermal structure is approximately proportional to radiative losses. This result is consistent with our detailed analysis of the loop system, feature (a). If feature (b) is in fact the base of a very high loop so that gravitational term is not required, then radiative losses also predominate at all locations and the above relationship also applies. A heating mode depending on the square of the local pressure is, however, not consistent with typical wave mode energy dissipation rates (Rosner, Tucker, and Vaiana, 1978; Craig, McClymont, and Underwood, 1978) nor with the constant volumetric heating rate adopted by Vesecký, Antiochus, and Underwood (1979).

6. Summary

We have examined a large and relatively cool coronal loop system associated with a decaying active region and a large near-radial feature that may be either the base of a very large loop or the base of a helmet streamer. In each case we find that radiative losses are far greater than the divergence of the conductive flux so that energy deposition proportional to the square of the electron density (or pressure) best fit the observations. This result imposes an additional constraint on possible heating processes for these cool coronal loops. Such heating must be distributed along the loops and not be localized to the loop tops. We also point out that observed geometry of diverging loops connecting to distant weak field regions appears to be incompatible with the twisting of magnetic field lines and subsequent reconnection and energy release.

Acknowledgements

WMN wishes to thank E. Hildner and his staff at NOAA's Space Environment Center for their hospitality and technical support to him as a guest worker. His work was supported by NASA Contract NAS5–32350 with the Raytheon STX Corp. We also thank the EIT and LASCO technical staff at SOHO's Experiment Operations Facility, with particular acknowledgment to E. Einfalt and S. Stezelberger, for their dedication in planning and executing the observational schedule for the EIT. We thank the anonymous referee whose comments improved the final manuscript. SOHO is a project of international cooperation between ESA and NASA.

References

Arndt, M. B., Habbal, S. R., and Karovska, M.: 1994, *Solar Phys.* **150**, 165.

Aschwanden, M. J., Neupert, W. M., Newmark, J., Thompson, B. J., Brosius, J. W., Holman, G. D., Harrison, R. A., Bastian, T. S., Nitta, N., Hudson, H. S., and Zucker, A.: 1998a, *Publ. Astron. Soc. Pacific*, to appear.

Aschwanden, M. J., Newmark, J. S., Delaboudinière, J.-P., Neupert, W. M., Klimchuk, J. A., Gary, G. A., Portier-Fozzani, F., and Zucker, A. : 1998b, *Astrophys. J.*, submitted.

Brekke, P., Kjeldseth-Moe, O., Brynildsen, N., Maltby, P., Haugan, S. W. H., Harrison, R. A., Thompson, W. T., and Pike, C. D.: 1997, *Solar Phys.* **170**, 163.

Cargill, P. J. and Klimchuk, J. A.: 1997, *Astrophys. J.* **478**, 799.

Craig, J. D., McClymont, A. N., and Underwood, J. H.: 1978, *Astron. Astrophys.* **70**, 1.

Defise, J. M., Clette, F., Moses, J. D., Hochedez, J.-F and the EIT Consortium: 1997, *Soc. Photo-Optical Instr. Eng.* **3114**, 598.

Delaboudinière J.-P., Artzner, G. E., Brunaud, J., Gabriel, A. H., Hochedez, J. F., Millier, F., Song, X. Y., Au, B., Dere, K. P., Howard, R. A., Kreplin, R., Michels, D. J., Moses, J. D., Defise, J. M., Jamar, C., Rochus, P., Chauvineau, J. P., Marioge, J. P., Catura, R. C., Lemen, J, R., Shing, L., Stem, R. A., Gurman, J. B., Neupert, W. M., Maucherat, A., Clette, F., Cugnon, P., and Van Dessel, E. L.: 1995, *Solar Phys.* **192**, 29.

Dere, A., Landi, E., Mason, H. E., Monsignori-Fossi, B. C., and Young, P. R.: 1996, *Astron. Astrophys. Suppl. Ser.* **125**, 149.
Feldman, W. C., Habbal, S. R., Hoogeveen, G., and Wang, Y.-M.: 1997, *J. Geophys. Res.* **102**, (A12), 26905.
Golub, L., Herant, M., Kalata, K., Lovas, I., Nystrom, G., Pardo, F., Spiller, E., and Wilcynski, J.: 1990, *Nature* **344**, 842.
Kano, R. and Tsuneta, S.: 1995, *Astrophys. J.* **454**, 934.
Klimchuk, J. A. and Gary, D. E.: 1995, *Astrophys. J.* **448**, 925.
Klimchuk, J. A. and Porter, L. J.: 1995, *Nature* **377**, 131.
Klimchuk, J. A., Lemen, J. R., Feldman, U., Tsuneta, S., and Uchida, Y.: 1992, *Publ. Astron. Soc. Japan* **44**, L181.
Kopp, R. A. and Orrall, F. Q.: 1976, *Astron. Astrophys* **53**, 363.
Moses, D., Clette, F., Delaboudinière, J.-P., Artzner, G. E., Brunaud, J., Carabetian, C., Gabriel, A. H., Hochedez, J. F., Millier, F., Song, X. Y., Au, B., Dere, K. P., Howard, R. A., Kreplin, R., Michels, D. J., Defise, J. M., Jamar, C., Rochus, P., Chavineau, J. P., Marioge., J. P., Catura, R. C., Lemen, J. R., Shing, L., Stem, R. A., Gurman, J. B., Neupert, W. M., Newmark, J., Thompson, B., Maucherat, A., Portier- Fozzani, F., Berghmans, D., Cugnon, P., Van Dessel, E. L., and Gabryl, J. R.: 1997, *Solar Phys.* **175**, 571.
Newmark, J.: 1996, EOS **77** (46), F557.
Plunkett, S.: 1996, private communication.
Pneuman, G. W. and Kopp, R. A.: 1997, *Astron. Astrophys.* **55**, 305.
Porter, L. J. and Klimchuk, J. A.: 1995, *Astrophys. J.* **454**, 499.
Portier-Fozzani, F., Neupert, W. M., Aschwanden, M., Sheeley, N. R., Thompson, B., Maucherat, A. J., Newmark, J., Klimchuk, J. and the EIT Team: 1998, Publ. Astron. Soc. Pacific, to appear.
Rosner, R., Tucker, W. H., and Vaiana, G. S.: 1978, *Astrophys. J.* **220**, 643.
Sams, B. J. III, Golub, L., and Weiss, N. O.: 1992, *Astrophys. J.* **399**, 313.
Sheeley, N. R., Jr.: 1980, *Solar Phys.* **66**, 79.
Tarbell, T.: 1996, private communication to the EIT Team.
Vesecký, J. F., Antiochus, S. K., and Underwood, J. H.: 1979, *Astrophys. J.* **233**, 987.
Walker, A. B. C., Barbee, T. W. Jr., Hoover, R. B., and Lindblom, J. F: 1988, *Science* **241**, 1781.
Webb, D. F.: 1981, in, F. Q. Orrall (ed.), *Solar Active Regions, A Monograph from Skylab Solar Workshop III*, Colorado Associated University Press, Boulder.
Wheatland, M. S., Sturrock, P. A., and Acton, L. W.: 1997, *Astrophys. J.* **482**, 510.
Withbroe, G. L.: 1988, *Astrophys. J.* **325**, 442.
Withbroe, G. L. and Noyes, R.: 1977, *ARA&A* **15**, 363.
Yoshida, T. and Tsuneta, S.: 1995, *Astrophys. J.* **459**, 342.